

Ultrafast Ultrasound Imaging Using Combined Transmissions With Cross-Coherence-Based Reconstruction

Yang Zhang, *Student Member, IEEE*, Yuexin Guo, *Student Member, IEEE*,
and Wei-Ning Lee, *Member, IEEE*

Abstract—Plane-wave-based ultrafast imaging has become the prevalent technique for non-conventional ultrasound imaging. The image quality, especially in terms of the suppression of artifacts, is generally compromised by reducing the number of transmissions for a higher frame rate. We hereby propose a new **ultrafast** imaging framework that **reduces not only the side lobe artifacts but also the axial lobe artifacts using combined transmissions with a new coherence-based factor**. The results from simulations, *in vitro* wire phantoms, the *ex vivo* porcine artery, and the *in vivo* porcine heart show that our proposed methodology greatly **reduced the axial lobe artifact** by 25 ± 5 dB compared with **coherent plane-wave compounding (CPWC)**, which **was considered as the ultrafast imaging standard**, and **suppressed side lobe artifacts** by 15 ± 5 dB compared with CPWC and coherent spherical-wave compounding. The **reduction of artifacts** in our proposed ultrafast imaging framework led to a better boundary delineation of soft tissues than CPWC.

Index Terms—Artifact, coherence, image reconstruction, plane wave, spherical wave, ultrafast, ultrasound.

I. INTRODUCTION

ULTRASOUND imaging is the predominant diagnostic imaging modality in the clinic for dynamic tissues, such as the heart and vessels. Conventional ultrasound imaging is realized by scanning the tissue with sequentially emitted focused beams, recording and processing backscattered signals from each transmission, and then reconstructing a two-dimensional (2D) image by stacking the beamformed signals. The frame rate of ultrasound imaging is thus limited by the number of transmissions needed to reconstruct a full-view image, and the frame rate typically ranges between

30 and 100 frames per second (fps) given tens or hundreds of transmitted beams in array configurations. However, such frame rates are insufficient to track fast vibrations in tissues, such as mechanical and electromechanical waves (1 to 10 m/s) present in the heart [1]. To capture such fast vibrations in biological tissues, researchers have aimed to reconstruct a full-view image by processing the backscattered signals from single or several wide field-of-view-transmitted unfocused waves, enabling the frame rate on the order of kHz, commonly referred to as ultrafast ultrasound imaging [2].

The ultrafast acquisition with a plane-wave (PW) illumination represents a pivotal change in medical ultrasound imaging from real-time implementation (tens fps) to the ultrafast category (kilohertz fps). In [3], an ultrafast imaging system (up to 10,000 frames/s) was developed with a single-plane ultrasonic wave transmission to track the propagation of a transient shear wave. Because of the ultrafast imaging sequence, propagation of the shear wave could be traced using 1,000–2,000 fps in gel-based phantoms. Another approach to reaching high frame rates (up to 3,750 fps for biological tissues at a depth of 200 mm) with PW transmissions was proposed in [4] and [5], in which limited diffraction beams were designed to receive the backscattered signals; the two-dimensional (2D) and three-dimensional (3D) images were reconstructed by processing the backscattered signals in the Fourier domain. While the frame rate of PW imaging reached the physical limits of medical ultrasound imaging, the image quality, such as the resolution and contrast, was degraded [2].

A significant improvement in image quality in high-frame rate imaging has been made by compounding techniques (summation of multiple transmissions), such as sparse synthetic aperture (SA) imaging [6], [7] and coherent plane-wave compounding (CPWC) [8], [9]. Ultrasound synthetic aperture imaging utilizes one spherical-wave (SW) transmission from each array element to generate a low-resolution image for each transmission. A final high-resolution image is obtained by coherent summation of all the low-resolution images. Spatial resolution and contrast can be achieved equivalent to the optimal multi-focus imaging because SA realizes two-way focusing. However, the frame rate is generally as low as the conventional focused ultrasound imaging since the number of SW transmissions is similar to that of focused beams. Sparse SA imaging with sparse distributed transmissions is

Manuscript received June 13, 2017; revised July 26, 2017; accepted July 26, 2017. Date of publication August 4, 2017; date of current version February 1, 2018. This work was supported in part by Hong Kong Research Grants Council under Grant ECS 739413E and in part by University Development Fund. (*Corresponding author: Wei-Ning Lee.*)

Y. Zhang and Y. Guo are with the Department of Electrical and Electronic Engineering, The University of Hong Kong, Hong Kong.

W.-N. Lee is with the Department of Electrical and Electronic Engineering, The University of Hong Kong, Hong Kong, and also with Medical Engineering Programme, The University of Hong Kong, Hong Kong (e-mail: wnlee@eee.hku.hk).

This paper has supplementary downloadable material available at <http://ieeexplore.ieee.org> provided by the authors. This includes videos that correspond to Fig. 8 (a)–(d). This material is 5.3 MB. Contact wnlee@eee.hku.hk for further questions about this work.

Color versions of one or more of the figures in this paper are available online at <http://ieeexplore.ieee.org>.

Digital Object Identifier 10.1109/TMI.2017.2736423

thereafter proposed to increase the frame rate. In [10], ultrafast imaging of the heart with a frame rate of 4,500 to 900 fps by coherently compounding one to five diverging waves (a number of virtual sources behind the subaperture of the array) can be realized. Similar to the coherent synthetic summation of ultrasonic images acquired with spherical waves or diverging waves, CPWC is proposed in [8] for very high frame rate ultrasonography and transient elastography. The coherent summation of beamformed radio-frequency (RF) data obtained by PW transmissions with different steering angles results in equivalent image quality to conventional multi-focus ultrasound imaging but at a frame rate that is 10 times higher. Imaging with CPWC outperforms conventional focused ultrasound imaging in various applications, such as blood or tissue motion estimation [11], [12], shear wave elasticity imaging [13], [14], contrast agent dynamics [15], neurovascular coupling [16], and parametric imaging [17].

Although it is a currently prevalent technique for ultrafast ultrasound imaging, CPWC is known to suffer from certain artifacts that degrade the image quality, especially when few transmissions are used. **One major drawback of CPWC is the axial lobe artifact in the range direction, which stems from the ghost echoes and was theoretically analyzed in [18] and [19] in a Row-Column array configuration for PW transmission.** A theoretical model based on spatial impulse response was derived to illustrate the origin of axial ghost echoes, which were attributed to the edge waves of the array caused by the discontinuity of apodization. Since the ghost echoes were behind the dominated backscattered signals, the artifacts in the range direction could be found in the beamformed images. Additionally, the axial lobe artifacts were analyzed in the case of CPWC [20], in which the axial lobe generation mechanism was described by the late-arriving signals. Another drawback of CPWC is the side lobe artifact caused by the off-axis clutters. Since there is no real transmit focus for single or several frames, the off-axis clutters will not be perfectly suppressed compared with the optimal multi-focus method. Thus, the side lobes in PW imaging are higher than those by the conventional multi-focus method when only a few transmissions are used for ultrafast acquisitions. Both the axial lobe artifact and side lobes in CPWC with few transmissions lower the image contrast.

Several techniques have been investigated to improve the quality of CPWC. To reduce axial lobe artifacts, an integrated transmit apodization with roll-off regions was proposed in [18] to reduce the ghost echoes in the Row-Column array. Another relevant study was based on the angular apodization of CPWC [21], and the relationship among apodization in conventional focused imaging, apodization in CPWC, and apodization in SA imaging was detailed. They argued that SA images were equivalent to optimally focused images, and the same weighting function used in conventional imaging could be applied as angular apodization in PW imaging but was defined over the entire angle sequence. However, the transmit apodization method increases the complexity of hardware implementation and may change the transmitted wavefront and lower the wave energy. For side lobe suppression, receive apodization methods, such as the Hanning window and

Tukey window, have been widely applied in ultrasound imaging. However, these conventional apodization methods compromise the spatial resolution. An alternative is the data-dependent weighting method. Adaptive beamforming techniques, such as the minimum variance adaptive beamformer [22]–[26] and coherence-based beamformer [27], [28], have been extensively applied to ultrasound imaging. The minimum variance (MV) beamformer has initially been demonstrated to outperform delay and sum (DAS) beamformer in terms of spatial resolution. Unlike the conventional apodizations with fixed weightings, the weightings of the aperture in the MV beamformer are data dependent and are calculated from the inverse of the aperture data covariance matrix. Since the data-dependent weightings help to preserve the signals from the focus and suppress the noise and interference from the clutter, image quality, especially the spatial resolution, of the beamformed images can be improved. However, the application of the MV beamformer in the clinical ultrasound imaging system remains limited. One potential limitation of the MV beamformer is the lack of robustness against the biased-assumed wavefield parameters, such as sound velocity errors, phase aberrations, and scattering assumptions [22]. To enhance the robustness of the MV beamformer, several approaches have been investigated, such as spatial smoothing, diagonal loading, and the coherent minimum variance pixel-based (MVPB) beamformer [23]. The spatial smoothing process divides the array into overlapping subarrays to enhance the robustness of the estimated covariance matrix. Diagonal loading was performed to regularize the main diagonal of the covariance matrix to avoid ill-conditioning and enhance the robustness of the estimated inverse covariance matrix. Coherent MVPB was developed to improve the data alignment and covariance matrix estimations. Coherence-based methods, such as the coherence factor (CF) weighting [27], [29], could improve the image contrast by enhancing the in-phase signals and suppressing the out-of-phase signals. Combining MV and CF weighting [30] results in the simultaneous improvement of spatial resolution and contrast. These data-dependent beamforming methods improved spatial resolution and contrast in both focused ultrasound and PW ultrasound imaging at the cost of computational complexity. In addition, a Joint Transmitting-Receiving (JTR) adaptive beamforming scheme for PW compounding was introduced [31]. In contrast to conventional adaptive beamforming techniques, which were applied on one aperture data, JTR was applied to the compounding procedure with the consideration of the data correlation information of different emissions. The JTR method combined with the minimum variance (MV) beamformer and eigenspace-based minimum variance beamformer (ESBMV) was shown to achieve higher imaging quality than conventional adaptive methods. This work demonstrated the advantage of the consideration of the correlation information among different emissions. Overall, to overcome the drawbacks of CPWC and SA imaging, a first attempt to combine the individual advantages of PW and SA imaging was made [32]. The adaptive combination of the 64-transmit PW imaging and 64-transmit synthetic aperture imaging improved the spatial resolution over PW and signal-to-noise ratio (SNR) over SA

with half the typical number of transmits. However, the previous combined technique was neither in the ultrafast scenario nor capable of suppressing the axial lobe artifacts and side lobes.

Although ultrafast imaging methods allow for much faster image acquisitions with improved image quality using adaptive beamforming techniques, the computational load is a bottleneck in the implementation in clinical systems. Instead of the time or space domain reconstruction, Fourier-based reconstruction [4], [33]–[35] and the utilization of the sparsity of ultrasound images [36]–[39] were proposed to increase the calculation speed while improving the image quality. In [4], Fourier domain reconstruction methods were first introduced in high-frame-rate imaging with limited diffraction beams. Lately, a Stolt's f-k migration reconstruction method in the frequency-wavenumber (f-k) domain was proposed in [33] to accelerate the computation based on Fast Fourier Transforms (FFTs) and provide comparable or better lateral resolution than [4]. In [34], the frequency domain beamforming (FDBF) compatible with the dynamic aperture and apodization was extended from focused beam imaging to PW imaging, leading to a four-fold reduction in the number of samples and computational load. In addition, compressed sensing reconstruction techniques have been introduced in ultrasound imaging to reduce the amount of data. In [36], a compressed beamforming has been applied to cardiac ultrasound data, achieving a nearly eightfold reduction in the sampling rate. In [37], reconstruction of the 3D ultrasound data with compressed sensing and dictionary learning shows a reduction of 20% to 80% from the original data size. In [38], a compressed-sensing-based SA was proposed to increase the frame rate of ultrasound imaging. Finally, a sparse reconstruction framework for Fourier-based PW imaging was proposed in [39] to utilize both the Fourier domain processing and the sparsity of images in the sparsifying domain for the improvement of image quality. However, these methods were based on either PW or diverging-wave transmissions.

This study aims at dealing with the tradeoff between the frame rate and image quality, especially in the aspect of artifact reduction, in ultrafast medical ultrasound imaging. Inspired by [31] and [32], we hereby propose a new ultrafast imaging framework. In transmission, combined transmissions with a PW illumination by full aperture and two diverging spherical waves by edge array elements are exploited to ensure the ultrafast acquisitions. In receive, the full aperture is used for each transmission. The ghost echoes in the backscattered signals by PW transmissions are reduced with the combined diverging SW transmissions. A new cross-coherence factor (CCF) is devised with delayed backscattered signals by combined transmissions to reduce artifacts caused by the side lobes. In our previous work [40], we preliminarily evaluated the proposed method in a simulation study. In this study, we revised the method by subaperture process and systematically analyzed the performance of the proposed imaging methodology in simulations, wire phantom experiments, the *ex vivo* porcine artery, and the *in vivo* porcine heart.

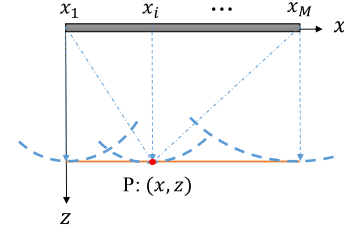


Fig. 1. Illustration of axial lobe formation.

II. METHODS

A. Theoretical Analysis of Axial Lobe Generation

The axial lobe formation can be explained based on the linear theory of wave propagation from a PW transmission by a linear array.

According to the linear theory of wave propagation [41], the acoustic pressure p at a given point P at the time t by the i -th array element is

$$p_i(P, t) = \rho_0 u(t) * \frac{\partial}{\partial t} h_i(P, t), \quad (1)$$

where $*$ denotes the temporal convolution operation, ρ_0 is the density of the medium, $u(t)$ is the convolution of the excitation signal and the electro-mechanical impulse response of the element, and $h_i(P, t)$ is the spatial impulse response of the i -th array element, which is the acoustic field at point P when the element is excited by a Dirac delta function.

The wave superposition property states that the acoustic field at any point in space generated by a linear array is constructed from the superposition of the acoustic field by all the individual elements. Thus, the pressure at point P by a linear array is

$$p(P, t) = \rho_0 u(t) * \frac{\partial}{\partial t} \sum_{i=1}^N (h_i(P, t)), \quad (2a)$$

$$= \rho_0 u(t) * \frac{\partial}{\partial t} h(P, t), \quad (2b)$$

where N is the number of array elements and $h(P, t)$ is the spatial impulse response of the array.

In conventional focused ultrasound imaging, all the signals (acoustic waves) emitted from the array elements arrive at the focus point P at the same time. However, in the PW transmission, all the array elements are excited at the same time, and some of the signals emitted by the elements of the array arrive at point P at different times. This effect is illustrated in Fig. 1, which illustrates the wavefront of the plane wave and the circular waves emitted from elements 1, i , and M . A planar wavefront, which is the superposition of the circular wavefronts from all emitted elements, reaches point P after a certain period of time:

$$t_p = z/c_0, \quad (3)$$

where c_0 is the speed of sound in the medium and the coordinate of point P is (x, z) . The arrival time of the circular wavefront from the i -th element at point P is

$$t_i = \sqrt{(x - x_i)^2 + z^2}/c_0, \quad (4)$$

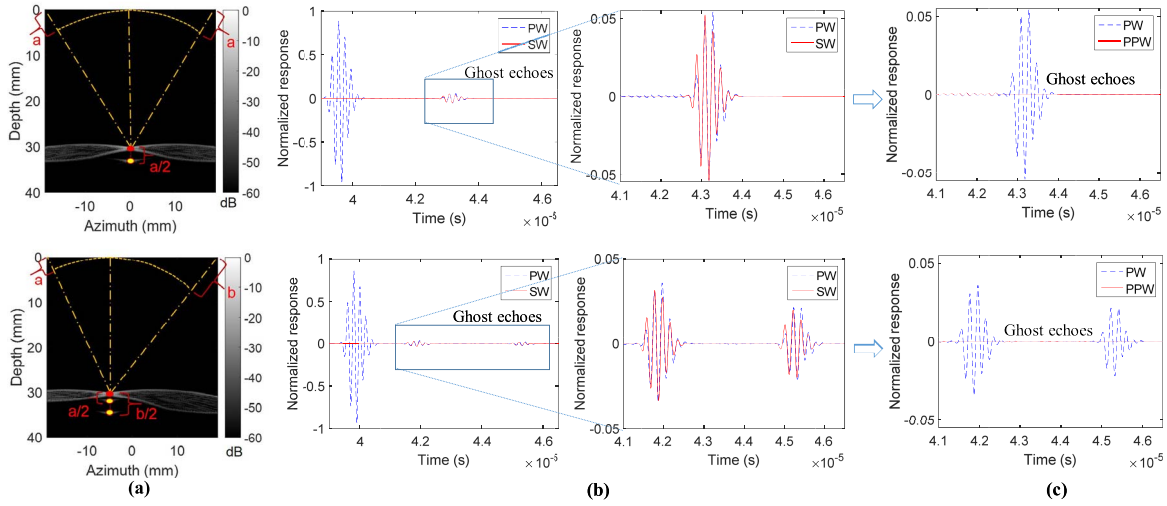


Fig. 2. Axial ghost echoes and axial lobe artifacts for centered (top panel) and off-centered (bottom panel) point targets: (a) the location of the axial lobe artifact in plane-wave (PW) imaging; (b) backscattered signals by PW and two averaged spherical-wave (SW) transmissions; (c) backscattered signals with suppressed ghost echoes. PPW denotes the preprocessed backscattered signal by PW.

where x_i is the x -coordinate of the i -th element. The delay between the circular wavefront by the i -th element and the planar wavefront is

$$\tau_i = (\sqrt{(x - x_i)^2 + z^2} - z)/c_0, \quad (5)$$

The late arrival of signals by elements with $x \neq x_i$ leads to delayed echoes that are observed behind the actual point target, leading to the axial lobes. For example, the plane wave and circular wave emitted by $i = 32$ arrive at point P simultaneously, so $\tau_{32} = 0$. However, the waves emitted by the elements 1 and 128 ($M = 128$) have not yet reached point P, so $\tau_1 > 0$, $\tau_{128} > 0$.

To identify the location and amplitude of the delayed echoes that cause axial lobes, we assume that the array is densely sampled and that the linear array can be simplified as a long and thin line element as in the Row-Column-Addressed array [18], [19]. According to the analysis of the spatial impulse response of the long and thin line element in [19], the spatial impulse response approximately satisfies

$$\frac{\partial}{\partial t} h(P, t) \propto \frac{d}{dt} a(x'(t)), \quad \text{if } t \geq t_p, \quad (6)$$

where a is the apodization function of the aperture, and it varies with a dependent variable position x' along the line element. a is equal to 0 when evaluated outside of the aperture surface.

By combining (6) and (2b), the pressure at point P by the linear array is proportional to

$$p(P, t) \propto \begin{cases} \rho_0 u(t) * \frac{d}{dt} a(x'(t)), & \text{if } t \geq t_p \\ 0, & \text{else} \end{cases} \quad (7)$$

A rectangular window results in constant apodization of the linear array over the entire array aperture. However, the apodization function evaluates to zero outside of the array area, and there is a discontinuity at the edges of the array elements 1 and M. Using the acoustic reciprocity, the time (t_p)

a planar wavefront takes from the linear array to arrive at point P is equivalent to the time that a wavefront emitted from the point P takes to travel along the shortest path to reach point x_p on the linear array. The first backscattered signal from point P would not be received until t_p . Thus, the time derivative of the apodization function is approximately zero everywhere except at the discontinuities at x_p , x_1 and x_M as follows:

$$\frac{d}{dt} a(x'(t)) \approx \delta(t - t_p) - \delta(t - t_1) - \delta(t - t_M). \quad (8)$$

Substituting (8) into (7) give three individual responses in the spatial impulse response of the array with $t_1 \neq t_M$. Next, there are three wavefronts that pass the point P with $t_1 \neq t_M$ but two wavefronts that pass the point P with $t_1 = t_M$.

The first wavefront arriving at time t_p is the major wavefront, which is planar. The second and third wavefronts ($t_1 \neq t_M$) form the observed delayed echoes (or ghost echoes) leading to axial lobe artifacts in the image. Since the ghost echoes are caused by the edge waves from the leftmost and rightmost array elements, their locations and amplitudes are comparable to the summed echoes by the edge array elements.

B. Reduction of Axial Lobe Artifacts

The locations of axial lobe artifacts in PW imaging (at 0 degrees) are shown in Fig. 2. A point target positioned at (x_s, z_s) leads to one apparent artifact when $x_s = 0$ or two apparent artifacts when $x_s \neq 0$. Using Field II simulation [42], the location of the axial lobe artifacts (x_g, z_g) was demonstrated to be consistent with the theoretical analysis and satisfies

$$2 \cdot |z_g - z_s| = \sqrt{(x_i - x_s)^2 + z_s^2} - |z_s|, \quad i = 1, \text{ or } N \quad (9)$$

where $(x_i, 0)$ is the coordinate of edge array elements, and N is again the total number of elements in the array probe. The center of the array probe is defined as $(0, 0)$. Note that $|x_1| = |x_N|$. When the point target lies in the central axis of the probe, in which $x_s = 0$, we can obtain

$(\mathbf{x}_1 - \mathbf{x}_s)^2 = (\mathbf{x}_N - \mathbf{x}_s)^2$, and the two artifacts from the two edges of the array are superpositioned to form one artifact. When the point target is deviated from the central axis of the array probe (i.e., $\mathbf{x}_s \neq \mathbf{0}$), we obtain $(\mathbf{x}_1 - \mathbf{x}_s)^2 \neq (\mathbf{x}_N - \mathbf{x}_s)^2$, and two distinct artifacts are present. Equation (9) describes that the distance between the apparent axial lobe artifact and the point target is half the differential distance between the point target and the closest element and the edge of the array.

Moreover, the backscattered signals by PW and SW transmissions are shown in Fig. 2 (b). The amplitude and phase of the ghost echoes by PW were found to be comparable to those of the echoes by SWs. This was consistent with the theoretical analysis of axial lobe generation. The simulation shows that the relationship between the ghost echoes by PW and echoes by SWs could be formulated as

$$g(t) \approx (s_l(t) + s_r(t))/2, \quad (10)$$

where $s_l(t)$ and $s_r(t)$ are the backscattered signals by two SW transmissions of edge array elements.

Since the axial lobe artifacts were confirmed to be attributed to the edge array elements, combined transmissions (1 PW and 2 SWs) were utilized to reduce the axial lobe artifacts in PW imaging. The main concept was to suppress the backscattered signal by PW with its high similarity to that by averaged SWs. The degree of similarity was quantified by the correlation coefficient between two backscattered signals from PW and SW transmissions. The calculation of the correlation coefficient was performed using segments of backscattered signals between two adjacent zero-crossing points, which preserved the phase continuity, as follows:

$$\begin{aligned} \rho_1(m, n) &= \frac{\sum_{n_1 < n < n_2} (s_{lr}(m, n) - \mu_{lr})(s_p(m, n) - \mu_p)}{\sqrt{\sum_{n_1 < n < n_2} (s_{lr}(m, n) - \mu_{lr})^2} \sqrt{\sum_{n_1 < n < n_2} (s_p(m, n) - \mu_p)^2}}, \end{aligned} \quad (11)$$

where index n indicates the n -th sample in the backscattered signals of the m -th channel, $s_{lr}(m, n)$ is the averaged backscattered signal by two SWs, $s_p(m, n)$ is the backscattered signal by PW, and μ_{lr} and μ_p are the average values of the backscattered signals by SW and PW, respectively. Each backscattered signal of the PW transmission was divided into multiple segments. Each segment was bound by two adjacent zero-crossing points— n_1 and n_2 . Such a segmented signal preserved the phase continuity and was therefore used to calculate its similarity (i.e., correlation coefficient) to the corresponding segment of the ghost echo signal.

The energy ratio between backscattered signals by PW and SW was

$$\rho_2(m, n) = \frac{\sum_{n_1 < n < n_2} s_{lr}^2(m, n)}{\sum_{n_1 < n < n_2} s_p^2(m, n)}, \quad (12)$$

As explained in theory that the ghost echoes (i.e., the axial lobe artifact in the B-mode) are caused by the edge waves of the array, they should be highly correlated with the backscattered signals of the SW transmissions from the edge array elements. However, the backscattered signals, except for the ghost echoes, of the PW transmission are decorrelated with

those of SW transmissions for the following reasons: First, the amplitude and phase of the backscattered signals depend on the scattered distribution of the medium, the excitation signal from each element, and positions of the active elements. Second, the active elements of the SW transmission are the edge array elements, which differ from the active elements of PW transmissions where full aperture are used. Finally, although the medium and excitation signal for each element are the same in PW and SW transmissions, the difference in the number and positions of the active elements causes the decorrelation of the backscattered signals from PW and SW transmissions except for the axial artifact positions.

The threshold values ϵ_1 and ϵ_2 were set to identify the ghost echoes in the backscattered signals. When ρ_1 was greater than or equal to a predefined threshold value $\epsilon_1 > 0$, and ρ_2 was smaller than or equal to a predefined threshold value $\epsilon_2 > 0$, the corresponding samples were considered ghost echoes and were suppressed by a multiplication factor of μ , which was used as the suppression ratio of the ghost echoes. When ρ_1 was smaller than the threshold value ϵ_1 , or ρ_2 was larger than the threshold value ϵ_2 , the samples remained unchanged. The final coefficient λ is then given by

$$\lambda = \begin{cases} \mu, & \rho_1 \geq \epsilon_1, \quad \rho_2 \leq \epsilon_2, \\ 1, & \text{Others} \end{cases} \quad (13)$$

The preprocessed backscattered signal by PW was the multiplication of the coefficient λ and the original signal. The selection of the threshold values ϵ_1 and ϵ_2 influences the identification of the ghost echoes. ϵ_1 is the lower bound of the correlation coefficient, and ϵ_2 is the upper bound of the energy ratio. μ is determined by the suppression ratio of the axial lobe artifacts. Fig. 2(c) shows the processed backscattered signal by PW.

C. Side Lobe Artifact Suppression

Side lobe artifacts are caused by the interference signal from the off-focus target. This type of artifact exists on the left and right sides of the imaging target as shown in Fig. 2(a). Since the interference signal from the off-focus target depends on the transmitted signals, the side lobe artifacts vary from different transmission settings. For example, the side lobe artifacts in the reconstructed B mode images by the PW transmission are different from those by the SW transmission. In DAS beamforming, each pixel in a B-mode image is obtained by the direct summation of the aperture data. The aperture data refer to the data received by each array channel after the focusing delays are applied. Therefore, the varied interference signal from off-focus target leads to the diversity of the aperture data from multiple transmissions. In this study, we designed a new factor, cross-coherence factor (CCF), to evaluate the similarity or the diversity of the aperture data from multiple transmissions. The larger the diversity is of the multiple aperture data, the smaller is the CCF. With CCF, the side lobe artifacts can be identified and suppressed.

The design of CCF was inspired by the Tanimoto coefficient [43], which measures the similarity and diversity

of two data sets:

$$c_0 = \frac{\sum_i x_i y_i}{\sum_i x_i^2 + \sum_i y_i^2 - \sum_i x_i y_i}. \quad (14)$$

where x_i and y_i are sample values of the two data sets to be compared, and i is from 1 to N , which is the total number of samples in each data set. To apply the Tanimoto coefficient to evaluate the similarity of two aperture datasets from two transmissions, all combinations of the samples in two aperture data need to be considered. Next, the formula was modified as

$$c'_{xy} = \frac{\sum_i \sum_j x_i y_j}{N(\sum_i x_i^2 + \sum_j y_j^2) - \sum_i \sum_j x_i y_j}, \quad (15)$$

Where N is then the total number of samples in one aperture dataset, and subscripts i, j are each from 1 to N .

It is known that

$$\begin{cases} \sum_i \sum_j x_i y_j = N^2 \mu_x \mu_y, \\ \sum_i x_i^2 = N(\sigma_x^2 + \mu_x^2), \\ \sum_i y_i^2 = N(\sigma_y^2 + \mu_y^2), \end{cases} \quad (16)$$

where μ_x and μ_y are the mean values of the aperture data, and σ_x and σ_y are the standard deviations. On substituting (16) into (15), we obtain

$$c'_{xy} = \frac{\mu_x \mu_y}{(\sigma_x^2 + \mu_x^2 + \sigma_y^2 + \mu_y^2) - \mu_x \mu_y}, \quad (17)$$

Calculation of c'_{xy} consists of the mean value and standard deviation of the two aperture data. In special cases, when the two aperture data are the same, c'_{xy} is

$$C'_{xy} = \frac{\mu_x^2}{(\mu_x^2 + 2\sigma_x^2)}. \quad (18)$$

Interestingly, the conventional coherence factor [27], [29] only considers single aperture data and is in the form

$$c_{xx} = \frac{|\sum_{i=1}^N x_i|^2}{N \sum_{i=1}^N |x_i|^2} = \frac{\mu_x^2}{\mu_x^2 + \sigma_x^2}. \quad (19)$$

The conventional coherence factor can be used as an index of focusing quality and can suppress the side lobe artifacts when it is used an adaptive weighting factor to each image sample. Since (19) only considers the coherence of single aperture data, c'_{xy} in (18) was further modified to be compatible with (19), as

$$c_{xy} = \frac{|\mu_x \mu_y|}{\mu_x^2 + \mu_y^2 - |\mu_x \mu_y| + (\sigma_x^2 + \sigma_y^2)/2}, \quad (20)$$

where c_{xy} denotes the designed CCF of two aperture data. When $\mu_x = \mu_y$ and $\sigma_x = \sigma_y$, c_{xy} is simplified to the conventional coherence factor [27], [29].

Furthermore, the spatial smoothing process could be applied to enhance the robustness of the c_{xy} calculation. The N element array was divided into $N-L+1$ overlapping subarrays, and the CCF based on the subarray process was

$$C_{xy} = \frac{1}{N-L+1} \sum_{l=1}^{N-L+1} c_{xlyl}, \quad (21)$$

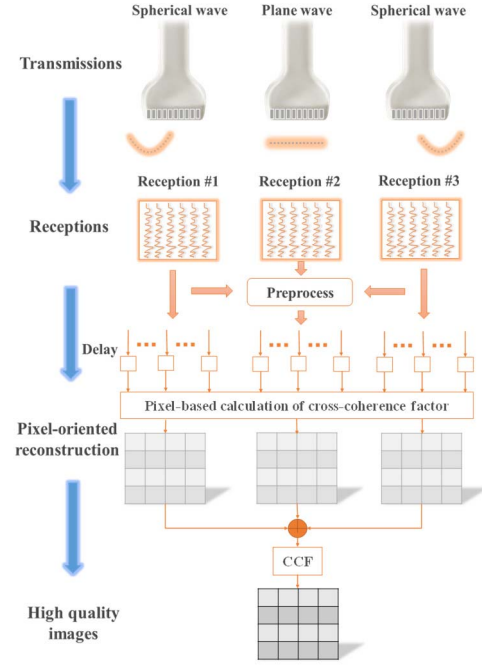


Fig. 3. Diagram of the proposed ultrafast ultrasound imaging framework, comprising combined transmissions, preprocessed backscattered signals, and coherence-based reconstruction.

where L is the number of elements in the subarray and l indicates the l -th element in the subarray. In this study, L represents half of the total number of elements of the full-sized array.

The proposed CCF for two aperture data can be obtained from (20) or (21) with spatial smoothing. When such a CCF is applied to M aperture data from M transmissions ($M > 2$), c_{xy} is computed from each pair in the M aperture data, constituting an M -by- M matrix as follows:

$$r = \begin{bmatrix} 1 & \cdots & c_{1M} \\ \vdots & \ddots & \vdots \\ c_{M1} & \cdots & 1 \end{bmatrix}. \quad (22)$$

The generalized CCF of multiple aperture data from multiple transmissions is thus

$$CCF = \sqrt{1 - \det(r)}. \quad (23)$$

The CCF serves as an index to measure the similarity of aperture data among multiple transmissions. Unlike the main lobes, the side lobes of the beamformed signals from different transmissions are different, so the CCF for the side lobe is much smaller than that for the main lobe. Thus, the side lobe artifacts can be suppressed when each image sample is weighted by its corresponding CCF. In this study, three transmissions were considered and thus $M = 3$.

D. Ultrafast Imaging Framework

The proposed ultrafast ultrasound imaging framework (Fig. 3) with combined transmissions and cross-coherence-based reconstruction (US-CTCC) comprises three parts: combined transmissions, preprocessed backscattered signals, and coherence-based reconstruction. An SW by the

leftmost edge array element, a PW by full aperture, and an SW by the rightmost edge array element are sequentially transmitted. Full aperture is applied in reception for each transmission event. As described in Section II-B, the CCF is calculated based on multiple aperture data consisting of preprocessed PW aperture data and SW aperture data. Next, a beamformed image comprising RF signals is reconstructed from the backscattered signals by two SWs and preprocessed backscattered signals by PW in six steps:

- 1) For each pixel in each transmission, the backscattered signals in each reception channel from each transmission are delayed to realize the dynamic receive focusing.
- 2) Next, for each pixel, the aperture domain signals for each transmission are obtained from the delayed backscattered signals in each reception channel.
- 3) The devised CCF (Section II-C) is calculated from the aperture domain signals for each pixel.
- 4) Low-quality beamformed signals are obtained by the summation of aperture domain signals for each pixel from each transmission.
- 5) The summation of the low-quality beamformed signals from PW and SW transmissions is weighted by the square root of the CCF for each pixel to obtain final beamformed RF data.
- 6) Beamformed RF data are envelope-detected to yield a B-mode image.

The physical limit of the frame rate for ultrafast ultrasound imaging depends on the velocity of ultrasound and acquisition depth. The acquisition frame rate can be achieved up to 15,000 frames/s for biological soft tissues (the velocity of ultrasound is 1,540 m/s) at a depth of 50 mm. In the proposed US-CTCC scheme, each image is obtained by compounding the three transmissions. Thus, the reconstruction frame rate would be 5,000 frames/s. However, when combined transmissions are successively transmitted and the backscattered signals are successively acquired, the reconstruction frame rate can remain at 15,000 frames/s by sliding the window for three combined transmissions. At such a frame rate, the vibration of soft tissues, for instance, shear waves, can be tracked.

III. RESULTS

A. Image Simulation and Experimental Setup

Simulations and the *in vitro* and *in vivo* experiments were conducted to test the performance of the proposed ultrafast imaging framework. CPWC (three angles: -7 degrees, 0 , 7 degrees, without transmit apodization) and coherent spherical-wave compounding (CSWC), in which three diverging spherical waves by leftmost, centered, and rightmost elements were transmitted and coherently summed to obtain the final ultrasonic images, were utilized as reference methods. The F number was 1.75.

1) *Ultrasound Image Simulation*: Simulations were performed using Field II [42] in MATLAB (The MathWorks, Natick, MA, USA). An L7-4 linear array probe (128 elements; 0.3-mm pitch) was modeled. The center frequency was 5.2 MHz, and the sampling frequency of the backscattered signals was 20.8 MHz. A point target phantom and a hollow

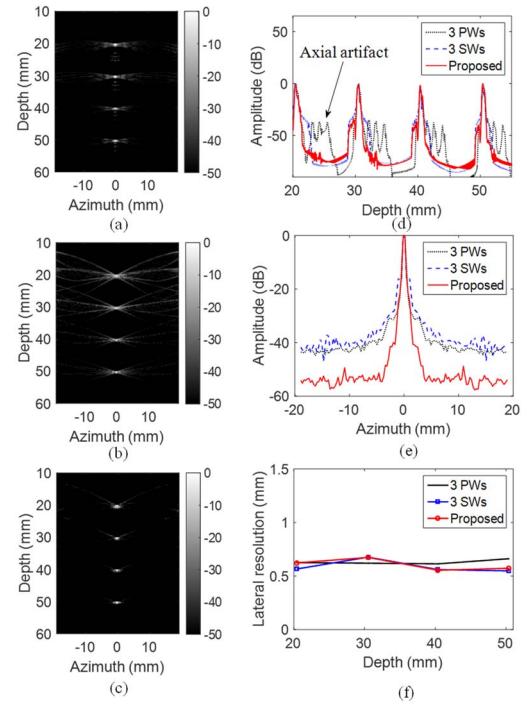


Fig. 4. Images of four point targets with a 50 dB dynamic range by (a) coherent compounding with three plane waves (3 PWs) at -7 degrees, 0 degrees, and 7 degrees, (b) coherent compounding with three spherical waves (3 SWs) from the leftmost, center, and rightmost elements, and (c) our proposed method with combined transmissions (US-CTCC). (d) and (f) are the axial profiles and the lateral resolutions of each point target. (e) shows the lateral profiles of the point target at 50 mm.

cylindrical phantom were separately simulated. Four point targets were positioned equally from 20 mm to 50 mm in depth. The hollow cylindrical phantom had a wall thickness of 4 mm and an inner diameter of 10 mm and was made comparable to the *ex vivo* porcine artery. Scatterers were randomly distributed with a density of 125 scatterers/mm², satisfying the requirement of fully developed speckle, and their amplitude followed the Gaussian distribution.

2) *Experimental Setup*: The data were acquired using a Verasonics Vantage 256 system with an ATL L7-4 probe (center frequency: 5.2 MHz; sampling rate: 20.8 MHz). Both a wire phantom and an *ex vivo* porcine artery were scanned. The wire phantom was made of four nylon wires spaced equally at 10 mm in water. A porcine aorta dissected from the porcine heart was placed in the saline bath. In addition, an open chest *in vivo* porcine heart was imaged to evaluate the performance of the proposed method. All animal procedures were approved prior to use by the Committee for the Use of Live Animals in Teaching & Research (CULATR) of the University of Hong Kong (Ref. No.: 3972-16).

B. Simulations

Figure 4 shows the B-mode images, axial and lateral profiles, and spatial resolutions of a simulated point target phantom using CPWC, CSWC, and the proposed US-CTCC method. Both axial lobe artifacts and side lobes were observed in the coherent compounded image with three plane waves.

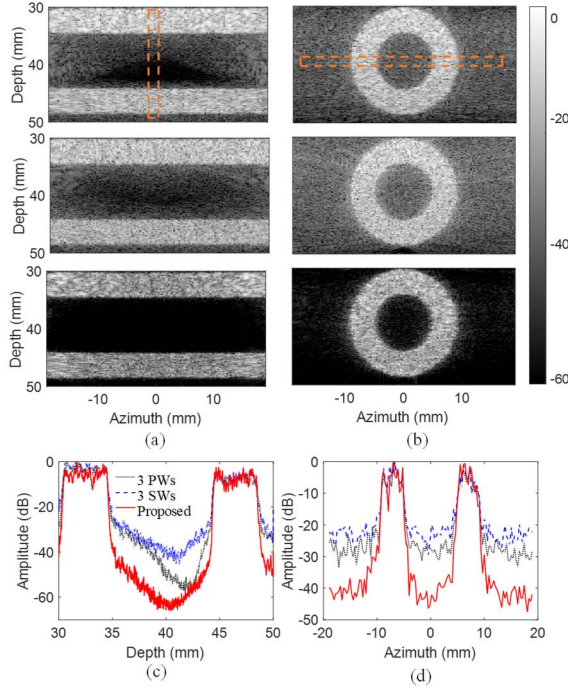


Fig. 5. Images of a simulated hollow cylindrical phantom in (a) the longitudinal view and (b) the transverse view displayed with a 60 dB dynamic range by (top) coherent compounding with three plane waves (3 PWs) at -7 degrees, 0 degrees, and 7 degrees, (middle) coherent compounding with three spherical waves (3 SWs) from the leftmost, center, and rightmost elements, and (bottom) our proposed method with combined transmissions (US-CTCC). (c) The axial profiles at the center of the hollow cylinder in the longitudinal view and (d) the lateral profiles of the cross-sectional image of the hollow cylinder at the imaging depth of 40 mm.

Side lobes were noted in CSWC imaging with three spherical waves. In this study, $\epsilon_1 = 0.1$, $\epsilon_2 = 10$, and $\mu = 0.02$ were utilized to suppress the axial lobe, and the proposed method was demonstrated to greatly reduce both axial lobe artifacts and side lobes. The axial and lateral profiles show that the reduction of the axial lobe artifact was 25 ± 5 dB compared with that by CPWC imaging, and the suppression of side lobes was approximately 15 dB compared with that by CPWC and CSWC imaging. The full width at half maximum (FWHM) of the point spread function (PSF) of each target was calculated as lateral resolutions (i.e., the size of the resolution cell) at each of the four different imaging depths. The lateral resolution remained at 0.6 mm.

The images and profiles of the simulated hollow cylindrical phantom in the longitudinal and transverse views are shown in Fig. 5. The reduction of artifacts in the lumen of the phantom by our proposed method was observed. The axial (Fig. 5(c)) and lateral (Fig. 5(d)) profiles show the reduction of artifacts by 20 ± 5 dB.

C. Wire Phantom Experiments

Figure 6 shows the B-mode images, axial and lateral profiles, and spatial resolutions of a wire phantom using CPWC imaging, CSWC imaging, and the proposed US-CTCC method. Fig. 6 (a) shows both the axial lobe artifacts and side lobes in CPWC (top), and the side lobes in CSWC

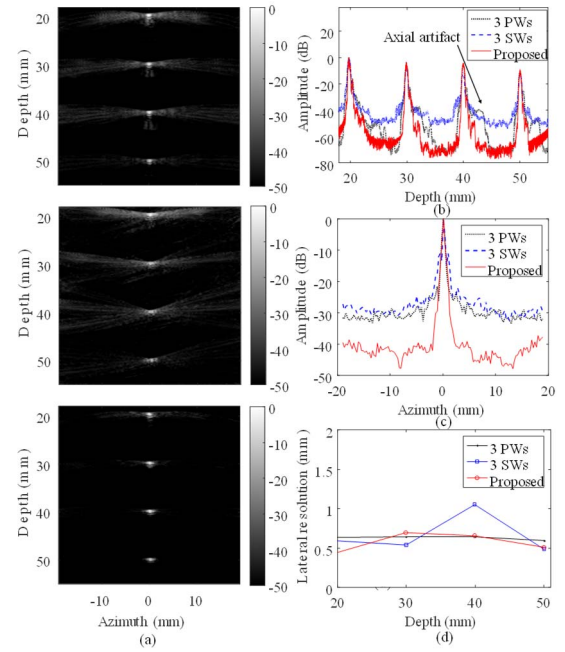


Fig. 6. (a) Images of a wire phantom displayed with a 50 dB dynamic range by (top) coherent compounding with three plane waves (3 PWs) at -7 degrees, 0 degrees, and 7 degrees, (middle) coherent compounding with three spherical waves (3 SWs) from the leftmost, center, and rightmost elements, and (bottom) our proposed method with combined transmissions (US-CTCC). (b) Axial profiles and (d) lateral resolutions measured from each point target and (c) lateral profiles of the point target at 50 mm in depth.

imaging with three spherical waves (middle). The proposed method (bottom) was demonstrated to greatly reduce both axial lobe artifacts and side lobes. The axial profiles in Fig. 6 (b) show that the reduction of axial lobe artifacts was 20 ± 5 dB compared with that by CPWC imaging, and the lateral profiles in Fig. 6 (c) show the suppression of side lobes by 15 ± 5 dB. The lateral resolution of the images in Fig. 6 (d) reconstructed by the proposed US-CTCC remained at 0.5 mm.

D. Ex Vivo Porcine Aorta Experiments

Figure 7 shows the images and profiles of the excised porcine aorta. The images of our proposed method show better boundary delineation than those by CPWC and CSWC imaging in both the longitudinal and transverse views. The reduction of artifacts in the lumen of the aorta was 10 ± 5 dB. The axial profiles in Fig. 7(e) show a lower artifact level in the lumen of the aorta than those in Fig. 7(d), where the electronic noise, instead of the side lobe and axial lobe artifacts, dominated. The signal to noise ratio (SNR) and contrast to noise ratio (CNR) were also calculated from the aorta images. Since the aorta was immersed in water, the SNR was calculated by the ratio between the vessel wall and water (blue boxes in Fig. 7.), where only noise was present. The SNR is defined as $SNR = 20 * \log_{10}(\mu_s/\mu_n)$, where μ_s and μ_n are the mean intensities of the regions in the vessel wall and water, respectively. The calculated SNR values for CPWC (3PWs), CSWC (3SWs), and US-CTCC were 45.5 dB, 30.4 dB, and 40.4 dB. Since combined transmissions were utilized, the proposed method had a slightly lower SNR

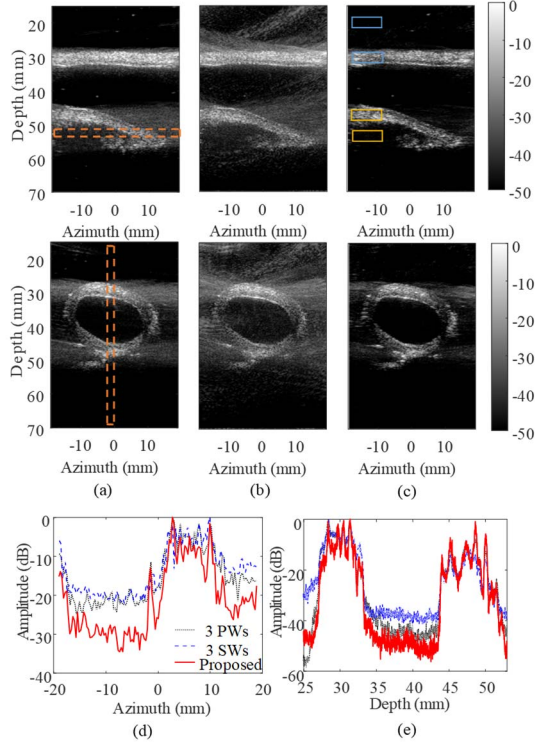


Fig. 7. Images of an excised porcine aorta with a 50 dB dynamic range in the longitudinal (top) and transverse (middle) views: (a) coherent compounding with three plane waves (3 PWs) at -7 degrees, 0 degrees, and 7 degrees, (b) coherent compounding with three spherical waves (3 SWs) from the leftmost, center, and rightmost elements, and (c) our proposed method with combined transmissions (US-CTCC). (d) Lateral and (e) axial profiles of the aorta images by three methods at the depth of 53.0 mm and an azimuthal position of 0 mm.

than the CPWC method, but a higher SNR than the CSWC method. The contrast to noise ratio was calculated by $CNR = |\mu_s - \mu_c| / \sqrt{\sigma_s^2 + \sigma_c^2}$, where μ_s and μ_c were respectively the mean intensities of the vessel wall and outside region, and σ_s and σ_c were the intensity standard deviations of the vessel wall and outside region. The regions for the calculation of CNR are delineated by the yellow boxes shown in Fig. 7. The calculated CNR values for 3PWs, 3SWs, and US-CTCC were 1.76, 1.71, and 1.34, respectively. The CNR values were lower with the US-CTCC, as the speckle variance increased due to the suppression of artifacts.

E. In Vivo Porcine Heart Experiments

Figure 8 shows the images of an *in vivo* porcine heart in both the long-axis and short-axis views in the systolic and diastolic phases. The proposed US-CTCC shows better boundary delineation of the left ventricular wall than CPWC. In addition, US-CTCC shows a better reduction of artifacts in the cavity than CPWC. Two videos of the US-CTCC images of the porcine heart in both long-axis and short-axis views over four consecutive cardiac cycles are available in the supplementary files /multimedia tab.

IV. DISCUSSION

In this study, ultrafast ultrasound imaging using combined plane- and spherical-wave transmissions with cross-coherence-based reconstruction (US-CTCC) was proposed. The proposed

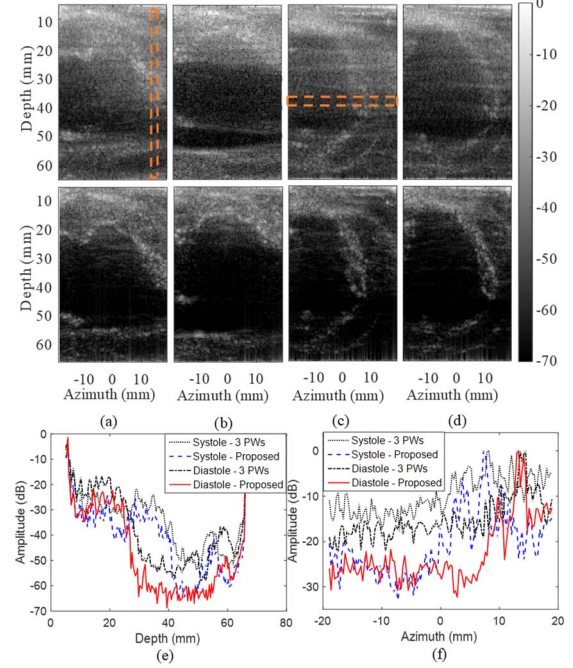


Fig. 8. Images of an *in vivo* porcine heart displayed with a 70 dB dynamic range in the long-axis view: (a) in systole with CPWC (top) and US-CTCC (bottom), (b) in diastole with CPWC (top) and US-CTCC (bottom), and the short-axis view: (c) in systole with CPWC (top) and US-CTCC (bottom), and (d) in diastole with CPWC (top) and US-CTCC (bottom). (e) and (f) are normalized axial and lateral profiles of the long-axis and short-axis views, respectively.

US-CTCC method as evaluated in simulations, a wire phantom, an *ex vivo* porcine aorta and an *in vivo* porcine left ventricle demonstrated the reduction of both axial lobe artifacts caused by the edge waves and side lobe artifacts caused by the off-axis clutters.

With the combined transmissions and preprocess procedure, the axial lobe artifacts caused by the edge waves by edge array elements in PW imaging could be reduced effectively. Similar to ghost echoes in row-column-addressed arrays [18], [19], the ghost echoes in backscattered signals by PW transmission are attributed to the discontinuity of the apodization of the linear array. The apodization function can be tapered to zero outside the linear array element area, causing a ghost wavefront in the pressure field. That the location and amplitude of the ghost echoes in backscattered signals by PW transmission are comparable to those of the backscattered signals by SW transmissions of edge array elements has offered the opportunity to separate the ghost echoes from the backscattered signals. Furthermore, in our study, both the cross-correlation coefficient and energy ratio between the backscattered signals by PW and SW transmissions were computed to measure the similarity between two waveforms. This provided a more robust estimation of the ghost echoes. Figs. 9(a)-(c) show simulated point spread functions from a flat PW transmission, PW transmission with Tukey window apodization and a flat PW with our proposed preprocess procedure, respectively. The simulation parameters were the same as those in Section III-A. The reduction of axial lobe artifacts by the preprocessing procedure was comparable to that by the transmit apodization

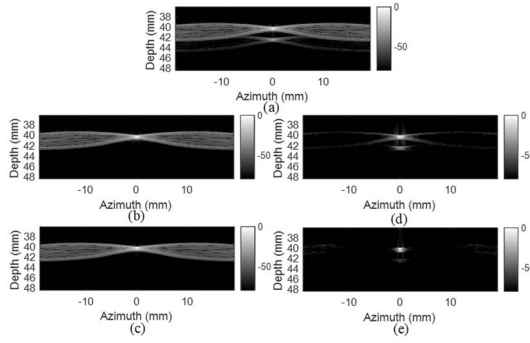


Fig. 9. Point spread function with a dynamic range of 80 dB by (a) single plane wave, (b) plane wave with transmit apodization, (c) plane wave with proposed preprocess procedure, (d) plane wave with conventional coherent factor method, and (e) plane wave with proposed cross-coherence factor method.

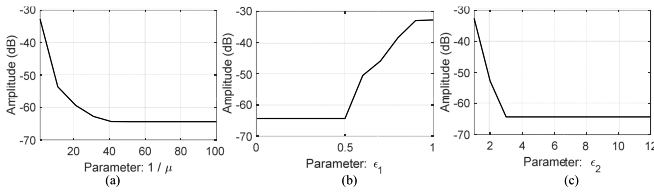


Fig. 10. The relationship between the axial lobe artifact level and the hyperparameter: (a) μ with $\epsilon_1 = 0.1$ and $\epsilon_2 = 10$, (b) ϵ_1 with $\mu = 1/50$, $\epsilon_2 = 10$, and (c) ϵ_2 with $\mu = 1/50$ and $\epsilon_1 = 0.1$ in (13) of our proposed preprocess procedure.

method. However, the transmit apodization method generally increases the hardware complexity and makes the transmitted wavefront planar only within the reduced beamwidth. In addition, hyperparameters in (13) regulate the performance of the suppression of axial lobe artifacts as either a monotonically increasing or decreasing function (Fig. 10). In this study, $\epsilon_1 = 0.1$, $\epsilon_2 = 10$, and $\mu = 0.02$ were selected for the suppressed artifact to be below -60 dB, for the low artifact level could be achieved at $0 < \epsilon_1 \leq 0.5$, $3 \leq \epsilon_2 \leq 12$, and $40 \leq 1/\mu \leq 100$.

Side lobes were suppressed by our devised CCF, which quantified the similarity of delayed backscattered signals among multiple frames. For each pixel, the backscattered signals were delayed based on dynamic receive focusing. Next, three aperture data sampled from the delayed backscattered signals in each receive channel were obtained. The similarity among different aperture data represented the confidence level of the coherently summed signals. This was similar to the analysis of side lobe suppression in [44] that the main lobe remained the same, while the side lobes varied with different apodizations and that the main lobes exhibited much higher similarity than side lobes among different aperture data. Thus, the degree of similarity reflected the likelihood of artifacts caused by side lobes. Our designed CCF has the property that the higher the similarity is among multiple frames, the larger is the factor. In addition, CCF is equivalent to the conventional coherence factor (CF) [29] when the two aperture data are the same. Conventional CF denotes the coherence of single aperture data and facilitates the assessment of focusing quality. In contrast, CCF not only measures the similarity among different aperture data but also evaluates the coherence

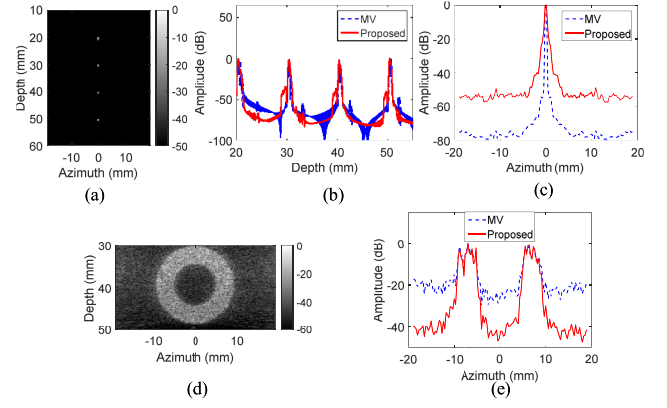


Fig. 11. Comparison between the MV beamformer and our proposed method in the case of simulated point targets: (a) B-mode image, (b) axial profiles, and (c) lateral profiles at 50 mm, and in the case of the cross-section of a simulated vessel phantom: (d) B-mode image, and (e) lateral profiles at 40 mm.

of each aperture data. Moreover, to compare the CCF with conventional CF, the simulated point spread functions by flat PW transmission are shown in Fig. 9(d) and Fig. 9(e). The side lobe artifacts are not apparent in the image after CCF weighting but remain in the image after CF weighting. CCF shows a higher capability of suppressing the side lobe artifacts than conventional CF.

The axial lobe and side lobe artifacts appear in different positions away from the targets. As shown in Fig. 4 and Fig. 6, the axial lobe artifacts are below the targets, while the side lobe artifacts are on the left and right sides. In the wire phantom, the axial lobe artifacts and side lobes are reduced by the preprocessing procedure and coherence-based reconstruction, respectively. However, the axial lobe artifacts and side lobes are intermingled in tissues, such as the lumen of the vessel. As shown in Fig. 5 and Fig. 7, both artifacts were present in the lumen of the artery. In this case, both the preprocess and coherence-based reconstruction likely reduced artifacts.

The proposed ultrafast imaging framework was demonstrated to exhibit comparable lateral resolution to CPWC and CSWC imaging. Unlike the Hanning window and Tukey window for the suppression of the side lobes through apodization, the coherence-based reconstruction method did not change the apodization or aperture size of the array so that it preserved the lateral resolution. Additionally compared with the widely-recognized MV beamformer, our proposed method achieved greater artifact reduction (Figs. 11 (d)-(e)). However, the MV beamformer is known to yield superior spatial resolution as evidenced in the case of point targets (Figs. 11 (a)-(c)). Nevertheless, the MV beamformer and our proposed method are not mutually exclusive but complementary because the former aims at the spatial resolution improvement and the latter focuses on artifact reduction. In addition, although the current implementation of the coherence-based reconstruction framework is in the spatial domain, the reconstruction is compatible with Fourier domain implementation to reduce the computation complexity. Furthermore, the proposed coherence-based reconstruction is not limited to ultrasound imaging and is envisioned to be applicable to other imaging

modalities that utilize array configuration, such as microwave imaging.

The feasibility of the new ultrafast imaging framework was tested in tissues of relatively simple geometry, such as the normal artery. Several limitations of our current framework remained. A relatively low sonographic SNR (SNRs) of the backscattered signals by SWs from edge array elements was noted. Owing to the relatively weaker energy of echoes from SW than that from PW, the SW was attenuated largely in the deeper region of the scanned medium. Increasing the SNRs will be investigated in future work. Another limitation is the alteration of the speckle variance in the image. The suppression of the axial lobe and side lobe artifacts will cause a larger speckle variance in the vessel wall. Despite the improved contrast between the vessel wall and lumen, the CNR was compromised by the increased standard deviation of the signal intensity, which was caused by the amplified alteration of the speckle pattern. This effect, however, has also been observed in other adaptive ultrasound imaging methods [22], [23], [30], [45], [46]. This phenomenon can be improved by spatial smoothing processing. The speckle pattern will also be a subject of future investigations. The added computational cost from the preprocess procedure and the calculation of the CCF for each pixel might be a potential concern in real-time ultrafast imaging. A sparsity strategy may be integrated into our proposed framework to reduce the computational load. Finally, the evaluation of our proposed ultrafast imaging framework was performed with three combined transmissions. In theory, the framework is expected to work as well with more than three transmissions (i.e., multiple tilted plane waves with two SWs by edge array elements). The axial lobe artifacts in each tilted plane wave can be reduced by the preprocessing procedure with two SWs by edge array elements, while the side lobes can be suppressed by the coherence-based reconstruction with CCF, which can be extended to the multiple-frame scenario.

V. CONCLUSIONS

We have investigated the feasibility of combined PW and SW transmissions with coherence-based reconstruction for ultrafast ultrasound imaging. The proposed US-CTCC framework was demonstrated to reduce both the axial lobe and side lobe artifacts compared with CPWC and CSWC imaging in simulations, a wire phantoms, an *ex vivo* porcine artery, and an *in vivo* porcine heart. Better boundary delineation and suppression of artifacts could be achieved by US-CTCC than CPWC. Future work includes the evaluation of this framework for ultrasound shear-wave imaging and **strain imaging**.

REFERENCES

- [1] A. P. Sarvazyan, O. V. Rudenko, S. D. Swanson, J. B. Fowlkes, and S. Y. Emelianov, "Shear wave elasticity imaging: A new ultrasonic technology of medical diagnostics," *Ultrasound Med. Biol.*, vol. 24, no. 9, pp. 1419–1435, 1998.
- [2] M. Tanter and M. Fink, "Ultrafast imaging in biomedical ultrasound," *IEEE Trans. Ultrason., Ferroelectr., Freq. Control*, vol. 61, no. 1, pp. 102–119, Jan. 2014.
- [3] L. Sandrin, S. Catheline, M. Tanter, X. Hennequin, and M. Fink, "Time-resolved pulsed elastography with ultrafast ultrasonic imaging," *Ultrason. Imag.*, vol. 21, no. 4, pp. 259–272, 1999.
- [4] J.-Y. Lu, "2D and 3D high frame rate imaging with limited diffraction beams," *IEEE Trans. Ultrason., Ferroelectr., Freq. Control*, vol. 44, no. 4, pp. 839–856, Jul. 1997.
- [5] J.-Y. Lu and J. F. Greenleaf, "Pulse-echo imaging using a nondiffracting beam transducer," *Ultrasound Med. Biol.*, vol. 17, no. 3, pp. 265–281, 1991.
- [6] J. A. Jensen, S. I. Nikolov, K. L. Gammelmark, and M. H. Pedersen, "Synthetic aperture ultrasound imaging," *Ultrasonics*, vol. 44, pp. e5–e15, Dec. 2006.
- [7] J. Kortbek, J. A. Jensen, and K. L. Gammelmark, "Sequential beam-forming for synthetic aperture imaging," *Ultrasonics*, vol. 53, no. 1, pp. 1–16, 2013.
- [8] G. Montaldo, M. Tanter, J. Bercoff, N. Benech, and M. Fink, "Coherent plane-wave compounding for very high frame rate ultrasonography and transient elastography," *IEEE Trans. Ultrason., Ferroelectr., Freq. Control*, vol. 56, no. 3, pp. 489–506, Mar. 2009.
- [9] B. Denarie *et al.*, "Coherent plane wave compounding for very high frame rate ultrasonography of rapidly moving targets," *IEEE Trans. Med. Imag.*, vol. 32, no. 7, pp. 1265–1276, Jul. 2013.
- [10] C. Papadacci, M. Pernot, M. Couade, M. Fink, and M. Tanter, "High-contrast ultrafast imaging of the heart," *IEEE Trans. Ultrason., Ferroelectr., Freq. Control*, vol. 61, no. 2, pp. 288–301, Feb. 2014.
- [11] B. F. Osmanski, M. Pernot, G. Montaldo, A. Bel, E. Messas, and M. Tanter, "Ultrafast Doppler imaging of blood flow dynamics in the myocardium," *IEEE Trans. Med. Imag.*, vol. 31, no. 8, pp. 1661–1668, Aug. 2012.
- [12] H. Li, Y. Guo, and W.-N. Lee, "Systematic performance evaluation of a cross-correlation-based ultrasound strain imaging method," *Ultrasound Med. Biol.*, vol. 42, no. 10, pp. 2436–2456, 2016.
- [13] P. Song, H. Zhao, A. Manduca, M. W. Urban, J. F. Greenleaf, and S. Chen, "Comb-push ultrasound shear elastography (CUSE): A novel method for two-dimensional shear elasticity imaging of soft tissues," *IEEE Trans. Med. Imag.*, vol. 31, no. 9, pp. 1821–1832, Sep. 2012.
- [14] P. Song, M. W. Urban, A. Manduca, H. Zhao, J. F. Greenleaf, and S. Chen, "Comb-push ultrasound shear elastography (CUSE) with various ultrasound push beams," *IEEE Trans. Med. Imag.*, vol. 32, no. 8, pp. 1435–1447, Aug. 2013.
- [15] J. R. Lindner, "Molecular imaging of cardiovascular disease with contrast-enhanced ultrasonography," *Nature Rev. Cardiol.*, vol. 6, no. 7, pp. 475–481, 2009.
- [16] E. Macé, G. Montaldo, I. Cohen, M. Baulac, M. Fink, and M. Tanter, "Functional ultrasound imaging of the brain," *Nature Methods*, vol. 8, no. 8, pp. 662–664, 2011.
- [17] X. Yu, Y. Guo, S.-M. Huang, M.-L. Li, and W.-N. Lee, "Beamforming effects on generalized Nakagami imaging," *Phys. Med. Biol.*, vol. 60, no. 19, p. 7513, 2015.
- [18] T. L. Christiansen, M. F. Rasmussen, J. P. Bagge, L. N. Moesner, J. A. Jensen, and E. V. Thomsen, "3-D imaging using row-column-addressed arrays with integrated apodization—Part II: Transducer fabrication and experimental results," *IEEE Trans. Ultrason., Ferroelectr., Freq. Control*, vol. 62, no. 5, pp. 959–971, May 2015.
- [19] M. F. Rasmussen, T. L. Christiansen, E. V. Thomsen, and J. A. Jensen, "3-D imaging using row-column-addressed arrays with integrated apodization—Part I: Apodization design and line element beamforming," *IEEE Trans. Ultrason., Ferroelectr., Freq. Control*, vol. 62, no. 5, pp. 947–958, May 2015.
- [20] A. Rodriguez-Molares, J. Avdal, H. Torp, and L. Løvstakken, "Axial lobes in coherent plane-wave compounding," in *Proc. IEEE Int. Ultrason. Symp. (IUS)*, Sep. 2016, pp. 1–4.
- [21] A. Rodriguez-Molares, H. Torp, B. Denarie, and L. Løvstakken, "The angular apodization in coherent plane-wave compounding [correspondence]," *IEEE Trans. Ultrason., Ferroelectr., Freq. Control*, vol. 62, no. 11, pp. 2018–2023, Nov. 2015.
- [22] J. F. Synnevag, A. Austeng, and S. Holm, "Adaptive beam-forming applied to medical ultrasound imaging," *IEEE Trans. Ultrason., Ferroelectr., Freq. Control*, vol. 54, no. 8, pp. 1606–1613, Aug. 2007.
- [23] N. Q. Nguyen and R. W. Prager, "Minimum variance approaches to ultrasound pixel-based beamforming," *IEEE Trans. Med. Imag.*, vol. 36, no. 2, pp. 374–384, Feb. 2016.
- [24] Z. Wang, J. Li, and R. Wu, "Time-delay- and time-reversal-based robust capon beamformers for ultrasound imaging," *IEEE Trans. Med. Imag.*, vol. 24, no. 10, pp. 1308–1322, Oct. 2005.

- [25] S. Mehdizadeh, A. Austeng, T. F. Johansen, and S. Holm, "Eigenspace based minimum variance beamforming applied to ultrasound imaging of acoustically hard tissues," *IEEE Trans. Med. Imag.*, vol. 31, no. 10, pp. 1912–1921, Oct. 2012.
- [26] J.-F. Synnevåg, A. Austeng, and S. Holm, "Benefits of minimum-variance beamforming in medical ultrasound imaging," *IEEE Trans. Ultrason., Ferroelect., Freq. Control*, vol. 56, no. 9, pp. 1868–1879, Sep. 2009.
- [27] P.-C. Li and M.-L. Li, "Adaptive imaging using the generalized coherence factor," *IEEE Trans. Ultrason., Ferroelect., Freq. Control*, vol. 50, no. 2, pp. 128–141, Feb. 2003.
- [28] C.-I. C. Nilsen and S. Holm, "Wiener beamforming and the coherence factor in ultrasound imaging," *IEEE Trans. Ultrason., Ferroelect., Freq. Control*, vol. 57, no. 6, pp. 1329–1346, Jun. 2010.
- [29] K. W. Hollman, K. W. Rigby, and M. O'Donnell, "Coherence factor of speckle from a multi-row probe," in *Proc. IEEE Ultrason. Symp.*, vol. 2, Oct. 1999, pp. 1257–1260.
- [30] B. M. Asl and A. Mahloojifar, "Minimum variance beamforming combined with adaptive coherence weighting applied to medical ultrasound imaging," *IEEE Trans. Ultrason., Ferroelect., Freq. Control*, vol. 56, no. 9, pp. 1923–1931, Sep. 2009.
- [31] J. Zhao, Y. Wang, X. Zeng, J. Yu, B. Y. S. Yiu, and A. C. H. Yu, "Plane wave compounding based on a joint transmitting-receiving adaptive beamformer," *IEEE Trans. Ultrason., Ferroelect., Freq. Control*, vol. 62, no. 8, pp. 1440–1452, Aug. 2015.
- [32] K. Kotowick, R. Rohling, and L. Lampe, "Adaptive compounding of synthetic aperture and compounded plane-wave imaging for fast ultrasonography," in *Proc. IEEE 10th Int. Symp. Biomed. Imag.*, Apr. 2013, pp. 784–787.
- [33] D. Garcia, L. Le Tarnec, S. Muth, E. Montagnon, J. Porée, and G. Cloutier, "Stolt's $f-k$ migration for plane wave ultrasound imaging," *IEEE Trans. Ultrason., Ferroelect., Freq. Control*, vol. 60, no. 9, pp. 1853–1867, Sep. 2013.
- [34] R. Cohen, Y. Sde-Chen, T. Chernyakova, C. Fraschini, J. Bercoff, and Y. C. Eldar, "Fourier domain beamforming for coherent plane-wave compounding," in *Proc. IEEE Int. Ultrason. Symp. (IUS)*, Oct. 2015, pp. 1–4.
- [35] M. Zhang *et al.*, "Extension of Fourier-based techniques for ultrafast imaging in ultrasound with diverging waves," *IEEE Trans. Ultrason., Ferroelect., Freq. Control*, vol. 63, no. 12, pp. 2125–2137, Dec. 2016.
- [36] N. Wagner, Y. C. Eldar, and Z. Friedman, "Compressed beamforming in ultrasound imaging," *IEEE Trans. Signal Process.*, vol. 60, no. 9, pp. 4643–4657, Sep. 2012.
- [37] O. Lorintiu, H. Liebgott, M. Alessandrini, O. Bernard, and D. Friboulet, "Compressed sensing reconstruction of 3D ultrasound data using dictionary learning and line-wise subsampling," *IEEE Trans. Med. Imag.*, vol. 34, no. 12, pp. 2467–2477, Dec. 2015.
- [38] J. Liu, Q. He, and J. Luo, "A compressed sensing strategy for synthetic transmit aperture ultrasound imaging," *IEEE Trans. Med. Imag.*, vol. 36, no. 4, pp. 878–891, Apr. 2016.
- [39] A. Besson *et al.*, "A sparse reconstruction framework for Fourier-based plane-wave imaging," *IEEE Trans. Ultrason., Ferroelect., Freq. Control*, vol. 63, no. 12, pp. 2092–2106, Dec. 2016.
- [40] Y. Zhang, Y. Guo, and W.-N. Lee, "Ultrafast imaging using combined transmissions with coherence-based reconstruction," in *Proc. IEEE Int. Ultrason. Symp. (IUS)*, Sep. 2016, pp. 1–4.
- [41] A. D. Pierce, *Acoustics: An Introduction to Its Physical Principles and Applications*. New York, NY, USA: McGraw-Hill, 1981.
- [42] J. A. Jensen, "Field: A program for simulating ultrasound systems," in *Proc. Med. Biol. Eng. Comput.*, vol. 4, 1996, pp. 351–353.
- [43] D. Bajusz, A. Rácz, and K. Héberger, "Why is Tanimoto index an appropriate choice for fingerprint-based similarity calculations?" *J. Cheminform.*, vol. 7, no. 1, p. 20, 2015.
- [44] C. H. Seo and J. T. Yen, "Sidelobe suppression in ultrasound imaging using dual apodization with cross-correlation," *IEEE Trans. Ultrason., Ferroelect., Freq. Control*, vol. 55, no. 10, pp. 2198–2210, Oct. 2008.
- [45] J.-F. Synnevåg, C.-I. C. Nilsen, and S. Holm, "P2b-13 speckle statistics in adaptive beamforming," in *Proc. IEEE Ultrason. Symp.*, Oct. 2007, pp. 1545–1548.
- [46] G. Matrone, A. S. Savoia, G. Caliano, and G. Magenes, "The delay multiply and sum beamforming algorithm in ultrasound B-mode medical imaging," *IEEE Trans. Med. Imag.*, vol. 34, no. 4, pp. 940–949, Apr. 2015.